



The impact of iterative reconstruction protocol, signal-to-background ratio and background activity on measurement of PET spatial resolution

Sahar Rezaei^{1,2} · Pardis Ghafarian^{3,4} · Mehrdad Bakhshayesh-Karam^{3,4} · Carlos F. Uribe⁵ · Arman Rahmim^{6,7} · Saeed Sarkar² · Mohammad Reza Ay^{1,2}

Received: 25 September 2019 / Accepted: 19 December 2019
© Japan Radiological Society 2020

Abstract

Objectives The present study aims to assess the impact of acquisition time, different iterative reconstruction protocols as well as image context (including contrast levels and background activities) on the measured spatial resolution in PET images.

Methods Discovery 690 PET/CT scanner was used to quantify spatial resolutions in terms of full width half maximum (FWHM) as derived (i) directly from capillary tubes embedded in air and (ii) indirectly from 10 mm-diameter sphere of the NEMA phantom. Different signal-to-background ratios (SBRs), background activity levels and acquisition times were applied. The emission data were reconstructed using iterative reconstruction protocols. Various combinations of iterations and subsets (it × sub) were evaluated.

Results For capillary tubes, improved FWHM values were obtained for higher it × sub, with improved performance for PSF algorithms relative to non-PSF algorithms. For the NEMA phantom, by increasing acquisition times from 1 to 5 min, intrinsic FWHM for reconstructions with it × sub 32 (54) was improved by 15.3% (13.2%), 15.1% (13.8%), 14.5% (12.8%) and 13.7% (12.7%) for OSEM, OSEM + PSF, OSEM + TOF and OSEM + PSF + TOF, respectively. Furthermore, for all reconstruction protocols, the FWHM improved with more impact for higher it × sub.

Conclusion Our results indicate that PET spatial resolution is greatly affected by SBR, background activity and the choice of the reconstruction protocols.

Keywords Positron emission tomography · FWHM · Spatial resolution · Iterative reconstruction · TOF · PSF

Introduction

The high specificity and sensitivity of oncological FDG PET/CT imaging have made it a mainstay of modern clinical imaging [1, 2]. Spatial resolution is one of the key

parameters impacting PET performance and interpretation in oncological imaging [3]. The proposed method for measuring the spatial resolution is straightforward in the NEMA standard [4] which is based on filtered back projection (FBP) algorithm and point source embedded in the air without

✉ Pardis Ghafarian
pardis.ghafarian@sbmu.ac.ir

¹ Department of Medical Physics and Biomedical Engineering, Tehran University of Medical Sciences, Tehran, Iran

² Research Center for Molecular and Cellular Imaging (RCMCI), Tehran University of Medical Sciences, Tehran, Iran

³ Chronic Respiratory Diseases Research Center, National Research Institute of Tuberculosis and Lung Diseases (NRITLD), Shahid Beheshti University of Medical Sciences, 19569-44413 Tehran, Iran

⁴ PET/CT and Cyclotron Center, Masih Daneshvari Hospital, Shahid Beheshti University of Medical Sciences, Tehran, Iran

⁵ Department of Functional Imaging, BC Cancer, Vancouver, BC, Canada

⁶ Departments of Radiology and Physics, University of British Columbia, Vancouver, Canada

⁷ Department of Integrative Oncology, BC Cancer Research Centre, Vancouver, Canada

scattering media. While the FBP algorithm is linear and desirable for systems with wide transaxial coverage [5, 6], the presence of gaps in sinogram data challenges FBP [7, 8]. Nowadays, iterative reconstruction algorithms are popular in PET imaging [9, 10]. Furthermore, iterative reconstruction algorithms have been improved by incorporating point spread function modeling (PSF) and time of flight (TOF). Reconstruction algorithms can affect the quantification of PET/CT images [11–13].

PET images reconstructed with PSF modeling and/or TOF result in improved PET-based quantification and can increase the SNR and contrast for lesions [14–16]. In patients with colorectal liver metastases, Rogasch et al. [17] showed that quantitative evaluation can be influenced when using either PSF or TOF protocols for radiotherapy or follow-up purposes in different tumor-to-background ratios. They also stated that PSF protocols showed the higher maximum standardized uptake value (SUV_{max}) at higher contrast, whereas in lower contrast TOF algorithms provided the higher SUV_{max} . It also illustrated that PSF modeling can improve the spatial resolution as well as diminish partial volume effects and provide more accurate SUV estimation [18–20]. Armstrong et al. [21] reported that PSF protocols can significantly increase the SUV measurement. They suggested that improvement of spatial resolution can be helpful in distinguishing normal and abnormal patterns in oncology [22, 23]. In general, improved spatial resolution can lead to accurate PET quantification as well as lesion detectability especially in small lesions with low uptake [24, 25].

A study [26] on patients with lung cancer reported that various PET biomarker have various sensitivities to reconstruction protocols. A previous work [27] investigated the influence of reconstruction and acquisition parameters on local noise in experimental phantoms and concluded that lower number of iterations or subsets can decrease the noise variance up to 80% in PET/CT images. Furthermore, they stated that higher filter values can reduce image noise up to 25%. Recent studies [28–31] have also shown that noise levels and artifacts can be substantially increased with decreasing acquisition times.

At this time, the measured FWHM in air cannot reflect the real measured FWHM values in practical situations, given the fact that the presence of background activity and contrast levels along with different reconstruction protocols can affect the measured FWHM in clinical PET/CT imaging. To address these challenges and achieve a more realistic spatial resolution measurement in clinical practice, we also used a 10 mm-diameter sphere of NEMA phantom for FWHM estimation. In the present study, only as a first step, the measured FWHM for the capillary tube in air in various reconstruction protocols was evaluated. In the next step, the impact of contrast, various acquisition times and background activities on the intrinsic FWHM

in scattering media was also evaluated with consideration of different reconstruction (PSF and/or TOF) protocols for 10 mm-diameter sphere of NEMA phantom.

Materials and methods

Experimental measurement

FWHM was measured for both capillary tubes in air and the NEMA phantom. In the first step, seven capillary tubes (inner diameter: 1 mm, length: 60 mm) filled with total activity 2 MBq of ^{18}F -FDG were positioned at scanner FOV according to the following locations (in centimeters): (x, y, z) : $(-20, 0, 0)$, $(-10, 0, 0)$, $(0, 0, 0)$, $(10, 0, 0)$, $(20, 0, 0)$, $(0, 0, -5.9)$ and $(0, 0, 5.9)$. In the second step, the three spheres of the NEMA phantom (10, 17 and 28 mm diameter) were filled with a solution of ^{18}F -FDG, using signal-to-background ratios (SBRs) of 2:1, 4:1 and 8:1. Two background activity concentrations (2.38 and 4.78 kBq/ml) were also used. The smallest sphere size (10 mm diameter) was utilized for the evaluation of the FWHM value.

Data acquisition and image reconstruction

In this study, we used a Discovery 690 PET/CT scanner (GE Healthcare, Milwaukee, Wisconsin, USA) equipped with a 64-slice CT scanner. This PET scanner uses lutetium yttrium oxyorthosilicate (LYSO) crystals with a 70 cm transaxial FOV. The coincidence time window of the PET scanner is 4.9 ns and timing resolution of TOF is 555 ps.

The PET data for both capillary tubes in air and the in-house-NEMA phantom were reconstructed with various reconstruction algorithms: (1) OSEM = OSEM with no PSF or TOF, (2) OSEM + PSF = OSEM with PSF only, (3), OSEM + TOF = OSEM with TOF only and (4) OSEM with PSF and TOF = OSEM + PSF + TOF. In capillary tubes, Gaussian post-smoothing filter of 0, 2, 3, 4, 5 and 6 mm in full width at half maximum (FWHM) was applied. For the NEMA phantom, no post-smoothing filter was used. The reconstruction parameters were 2 and 3 iterations, and 16 and 18 subsets for all reconstruction methods. The scans for all the SBRs used in this study were performed with a bed duration of 5 min for both the capillary tubes and the NEMA phantom. Additionally, for the NEMA phantom with $SBR=2:1$, various acquisition times (ranging from 1 to 5 min with a step of 1 min) were also used for various reconstruction protocols. CT imaging was obtained when 100 kVp, 80 mA and 1 s rotation time was utilized.

Assessment strategy

Spatial resolution was obtained as the FWHM in both radial and axial directions for each capillary tube. A parabolic fit was used to determine the maximum intensity pixel. Finally, linear interpolation between adjacent pixels specified the half-maximum points. Individual intrinsic FWHM values for different locations of capillary tubes were obtained by plotting $FWHM_{Measured}$ (FWHM measured in various reconstruction protocols) vs $FWHM_{Filter}$ (FWHM of Gaussian filters with various sizes) and a linear fit to the data was used to extrapolate to a post-reconstruction smoothing filter width of 0 mm (Eq. 1). This approach is preferable for improved accuracy [32] than using only the data with no post-smoothing. In the next step, $FWHM_{intrinsic}$ (FWHM of the PET system) was obtained by squared summation of all individual intrinsic values.

$$FWHM_{Measured}^2 = FWHM_{intrinsic}^2 + FWHM_{Filter}^2 \tag{1}$$

For the 10 mm-diameter sphere of the NEMA phantom, we determined intrinsic FWHM by applying the method in Hofheinz et al. [33]. This method performs convolution of a 3D isotropic Gaussian with the sphere geometry and derives the radial activity profile of a homogeneous sphere. The analytical solution contained some parameters such as true activity concentration within the sphere, the radius of a sphere, background level and FWHM of the Gaussian function. In this process, non-linear least squares fitting was used to determine FWHM of the Gaussian function. The remaining parameters were fixed to their known values. This method considers approximately similar values for the axial and transaxial resolution. The relative FWHM difference (%) was also applied for comparison of various iterative reconstruction protocols on the FWHM value.

Results

Table 1 summarizes the individual FWHM in various capillary tube locations embedded in the air when the lowest and the highest it × sub values were used for different reconstruction protocols. In each method, the smallest intrinsic FWHM was seen for the center of the FOV. In x, the individual intrinsic FWHM for the PSF algorithms (OSEM + PSF and OSEM + PSF + TOF) showed smaller values for higher it × sub, with the differences being greater in comparison to non-PSF protocols (OSEM and OSEM + TOF). It is also worth noting that the relative difference (%) between minimum and maximum of individual FWHM across different locations was 29.7% (28.4%), 34.1% (44.9%), 31.4% (32.4%) and 34.3% (44.6%) for OSEM, OSEM + PSF, OSEM + TOF and OSEM + PSF + TOF, respectively, when it × sub was 32 (54).

Figure 1 depicts intrinsic FWHM values as derived from capillary tubes embedded in the air in various reconstruction methods for a range of it × sub reconstructions. The higher it × sub yielded smaller FWHM values with more impact for PSF algorithms relative to non-PSF algorithms. The relative differences (%) between the minimum and maximum of FWHM values among different reconstruction algorithms were 13.6%, 18.0%, 24.4% and 27.0% when different it × sub (32, 36, 48 and 54) was considered, respectively.

The square of the measured FWHM vs the square of the FWHM of the Gaussian filter is plotted in Fig. 2. The relative differences (%) of the measured FWHM values for the minimum and maximum size of the post-smoothing filter when it × sub = 32 (54) were 28.0% (30.6%), 30.4% (43.2%), 29.1% (33.0%) and 32.8% (42.8%) for OSEM, OSEM + PSF, OSEM + TOF and OSEM + PSF + TOF, respectively.

Our findings related to intrinsic FWHM of the NEMA phantom for the various it × sub are shown in Fig. 3. The relative difference (%) between the minimum and maximum of intrinsic FWHM with increase in it × sub from 32 to 54, when 2:1, 4:1 and 8:1 SBR was applied, were 6.85%,

Table 1 Individual intrinsic FWHM values for different capillary tube locations embedded in the air and reconstruction protocols

Protocols		Location (x, y, z)						
Reconstruction method	It × sub	(- 20, 0, 0) (mm)	(- 10, 0, 0) (mm)	(0, 0, 0) (mm)	(10, 0, 0) (mm)	(20, 0, 0) (mm)	(0, 0, - 5.9) (mm)	(0, 0, 5.9) (mm)
OSEM	32	2.41	2.26	1.75	2.28	2.46	2.49	2.48
	54	2.32	2.06	1.66	2.10	2.31	2.28	2.27
OSEM + PSF	32	2.35	2.07	1.56	2.09	2.37	2.35	2.33
	54	1.36	1.33	1.19	1.34	1.39	2.16	2.13
OSEM + TOF	32	2.36	2.17	1.68	2.19	2.39	2.43	2.45
	54	2.21	1.83	1.52	1.84	2.23	2.25	2.23
OSEM + PSF + TOF	32	2.33	1.68	1.53	1.73	2.32	2.20	2.18
	54	1.32	1.27	1.18	1.29	1.36	2.13	2.12

Fig. 1 Intrinsic FWHM derived from capillary tubes embedded in the air for various reconstruction protocols as a function of iterations \times subsets

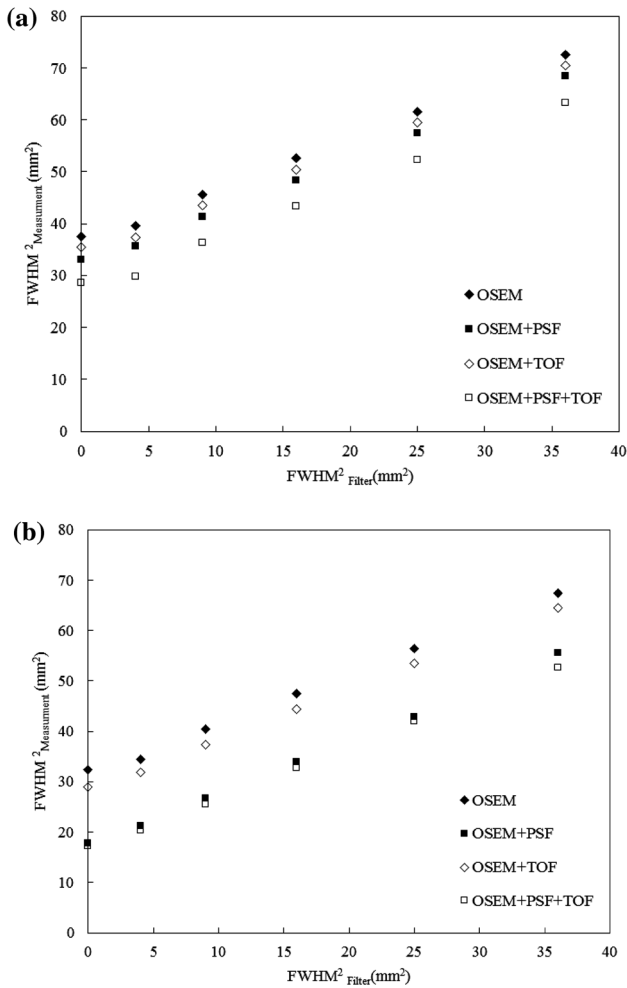
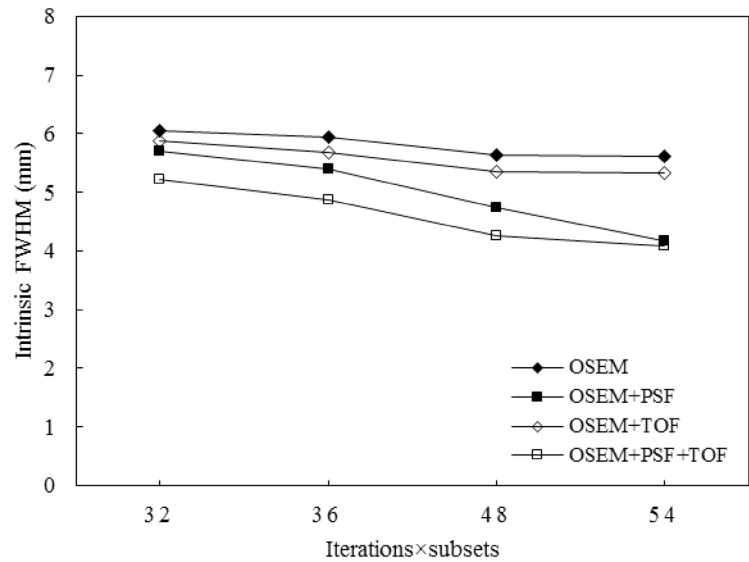


Fig. 2 Measured FWHM for capillary tubes embedded in the air as a function of post-smoothing Gaussian filter for different reconstruction protocols; **a** it \times sub = 32, **b** it \times sub = 54

8.88% and 7.33% for OSEM, 6.50%, 9.34% and 24.0% for OSEM + PSF, 6.12%, 11.6% and 9.16% for OSEM + TOF, and 7.67%, 14.7% and 21.6% for OSEM + PSF + TOF, respectively.

Variation of intrinsic FWHM in the NEMA phantom with SBR of 2:1 was evaluated when different acquisition times were applied (Fig. 4). The higher acquisition time yields improved intrinsic FWHM values. By increasing acquisition times from 1 to 5 min, intrinsic FWHM for it \times sub = 32 (54) was improved by 15.3% (13.2%), 15.1% (13.8%), 14.5% (12.8%) and 13.7% (12.7%) for OSEM, OSEM + PSF, OSEM + TOF and OSEM + PSF + TOF, respectively.

Figure 5 illustrates the impact of background variation on the intrinsic FWHM for the NEMA phantom when SBRs of 2:1 and 8:1 were used. For both low and high background activity and all reconstruction protocols, the FWHM improved when it \times sub increased. The relative differences (%) between the minimum and maximum intrinsic FWHM values for low (high) background activity was 5.28% (6.85%), 3.54% (6.50%), 5.00% (6.12%) and 5.23% (7.67%) for OSEM, OSEM + PSF, OSEM + TOF and OSEM + PSF + TOF, respectively, when it \times sub increased from 32 to 54 for 2:1 SBR and 7.17% (7.33%), 21.2% (24.0%), 8.86% (9.16%) and 19.5% (21.6%) for 8:1 SBR.

To evaluate the impact of the increasing it \times sub, the SNR (calculated as mean/SD) was measured for various SBRs (Fig. 6). An increase in it \times sub from 32 to 54 for OSEM, OSEM + PSF, OSEM + TOF and OSEM + PSF + TOF led to the SNR decreasing by 15.0%, 9.60%, 10.2% and 7.31%, respectively, for 2:1 SBR; 13.2%, 7.21%, 12.1% and 8.74%, respectively, for 4:1 SBR; and 21.9%, 13.9%, 19.1% and 14.2%, respectively, for 8:1 SBR.

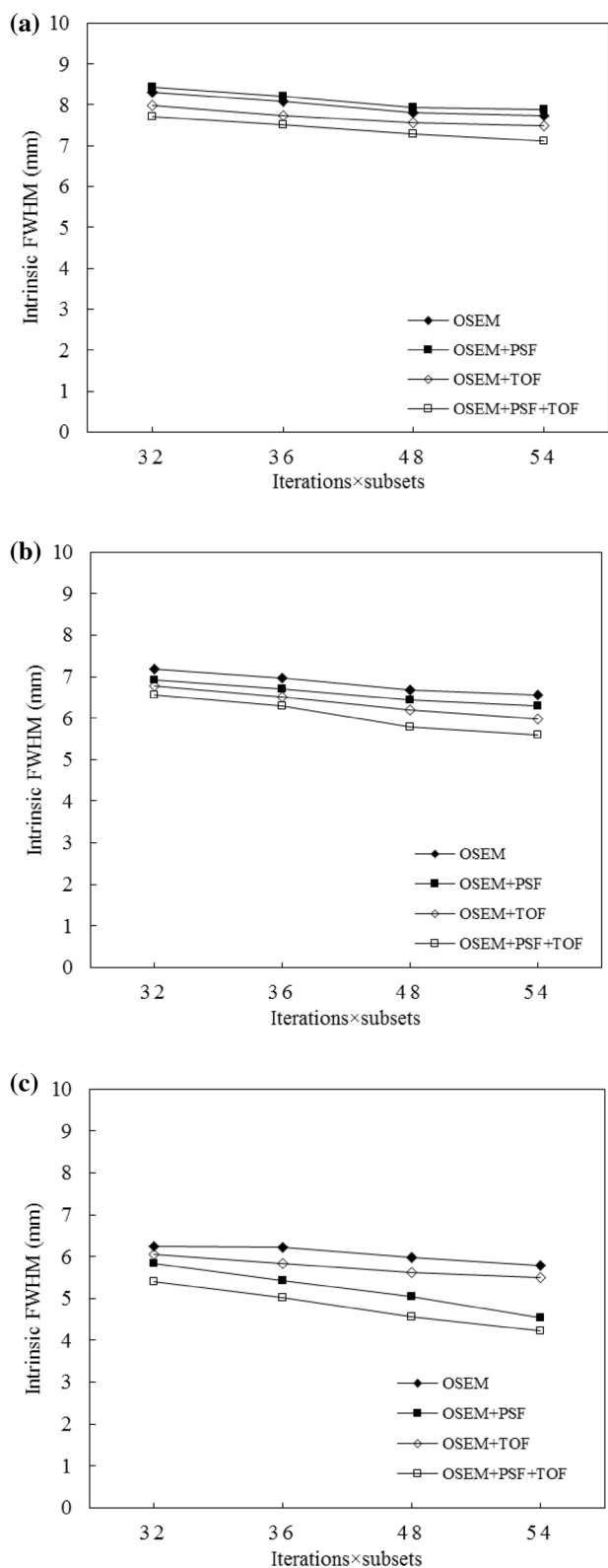


Fig. 3 Intrinsic FWHM measured from the NEMA phantom in various reconstruction protocols as a function of iterations x subsets; **a** SBR = 2:1, **b** SBR = 4:1 and **c** SBR = 8:1

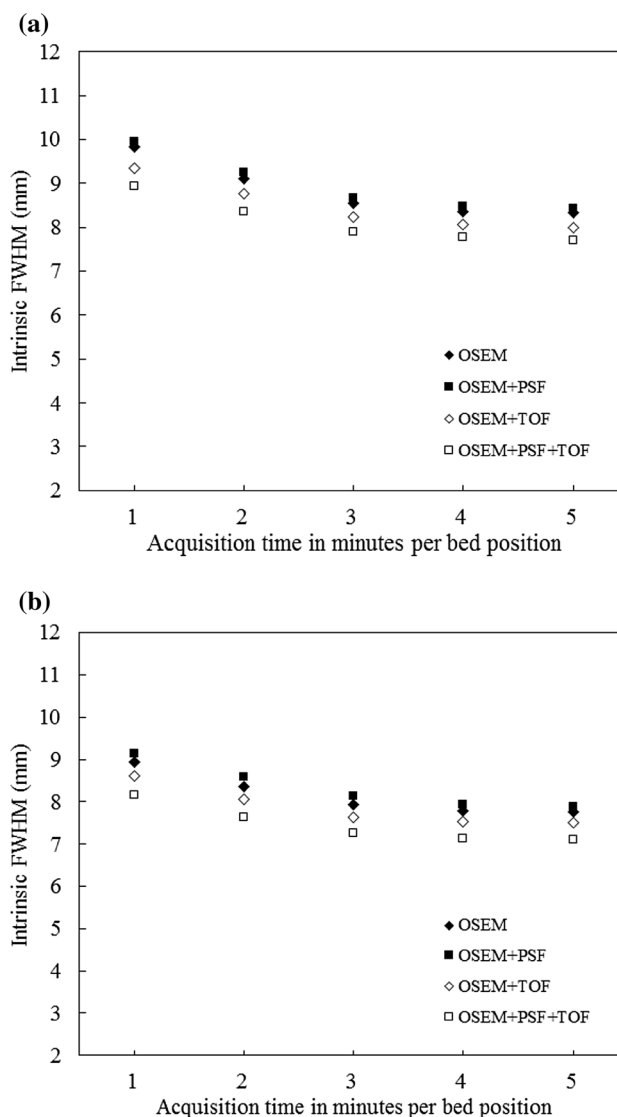


Fig. 4 Intrinsic FWHM derived from NEMA phantom for 1, 2, 3, 4 and 5 min acquisition time when SBR is 2:1; **a** it x sub = 32, **b** it x sub = 54

Discussion

In clinical PET/CT studies, the diagnostic quality is affected by the spatial resolution and noise levels of the image. Higher noise level can also effectively degrade spatial resolution and result in poorer accuracy. The choice of inappropriate reconstruction protocols [34–36] and low background activity [37] can lead to increased noise levels. Furthermore, the use of varying contrasts in spatial resolution measurement leads to contradictory measurements among studies [38]. To address these challenges, we assessed the influence of various reconstruction parameters, contrast and background activities for OSEM, OSEM + PSF, OSEM + TOF and OSEM + PSF + TOF for both capillary tubes embedded

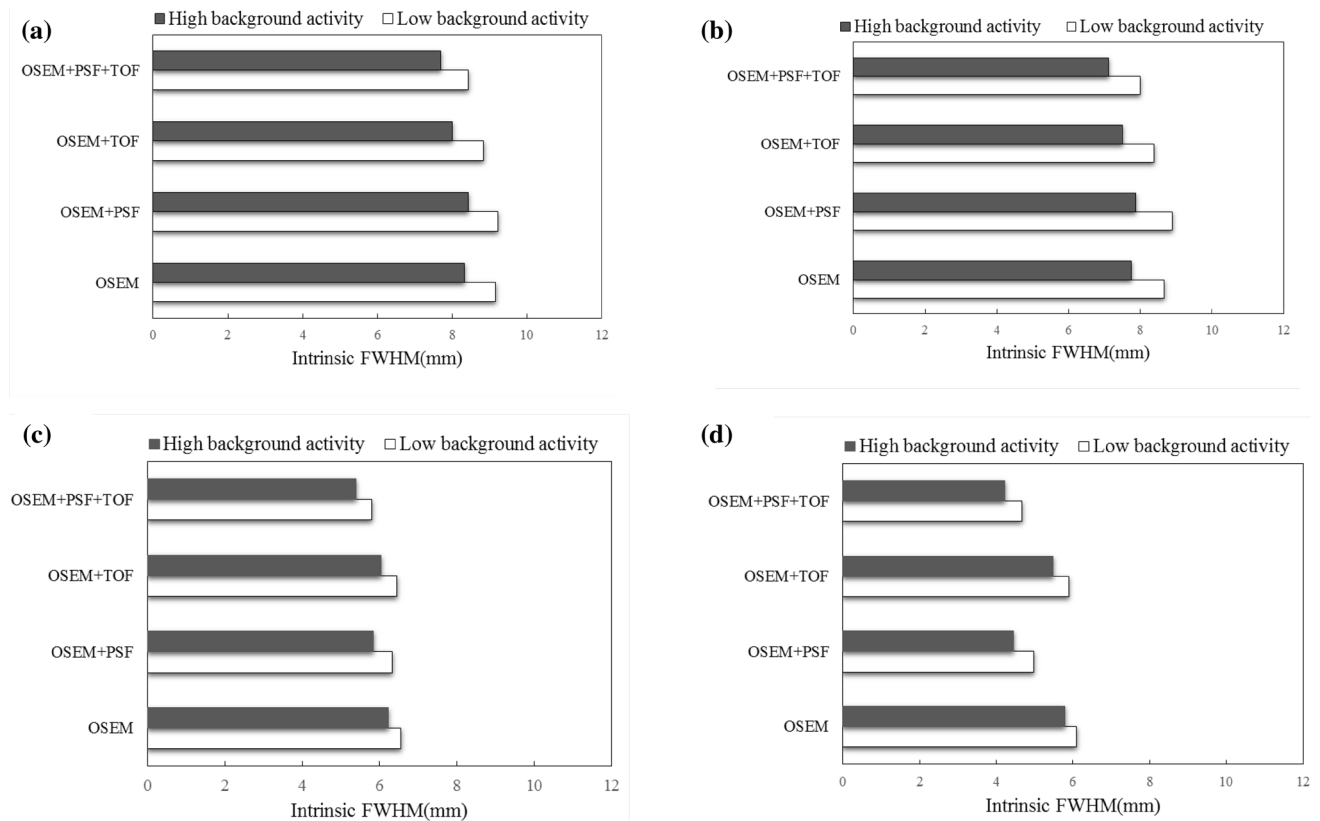


Fig. 5 Intrinsic FWHM derived from NEMA phantom when background activity levels were 2.38 kBq/mL and 4.78 kBq/mL. SBR = 2:1; **a** $it \times sub = 32$, **b** $it \times sub = 54$; SBR = 8:1; **c** $it \times sub = 32$, **d** $it \times sub = 54$

in the air and the NEMA phantom for measurement of FWHM in PET/CT images.

The PSF algorithm leads to better as well as more uniform spatial resolution throughout the FOV and can improve the image quality, due to incorporation of additional information about the detector system response within the system matrix of the iterative reconstruction algorithm [39]. At the same time, the more advanced reconstruction model of PSF algorithm needs more iterations to adequately reconstruct images. Our findings in capillary tubes depicted that the larger distance to the center of FOV results in a degraded individual FWHM with less impact on PSF algorithms versus to non-PSF algorithms (Table 1), as would be expected due to parallax effects. Although PSF algorithms can lead to improved individual FWHM values in different locations of scanner FOV relative to non-PSF algorithms, actually these algorithms are greatly sensitive to the choice of the reconstruction parameters (Table 1).

We also observed that intrinsic FWHM measurements in capillary tubes were improved by increase in $it \times sub$ (Fig. 1). The dependency of FWHM on reconstruction parameters is in agreement with previous studies showing that spatial resolution measurements can be affected by the number of iterations [38, 40]. In Fig. 1 with increase in $it \times sub$ from 32

to 54, the improvement in FWHM was 7.28%, 26.9%, 9.19% and 21.6% for OSEM, OSEM + PSF, OSEM + TOF and OSEM + PSF + TOF, respectively, which is in line with the findings of Lodge et al. [32] that demonstrated that FWHM values were not more affected by increasing the iteration numbers when applying the OSEM + TOF reconstruction algorithm (less than or equal to 5%). However, their reconstruction parameters showed some difference when compared to our parameters.

Our study revealed that (Fig. 2), with increase in the post-smoothing filter in capillary tubes, FWHM value was increased for various reconstruction protocols that are in line with previous studies [41, 42]. In addition, more attention must be applied to choosing filter size of higher $it \times sub$ when PSF protocols are applied. It seems interesting that when 5 mm post-smoothing filter was applied, and $it \times sub$ was 32 (54), the relative difference between OSEM and OSEM + PSF + TOF for the square of the measured FWHM was 15.1% (25.7%), respectively.

The non-linearity and the non-negativity constraint of the iterative reconstruction algorithms were a paramount cause for contrast-dependent spatial resolution [43, 44]. We observed that, for 10 mm sphere diameter of the NEMA phantom, intrinsic FWHM values improved for higher SBR

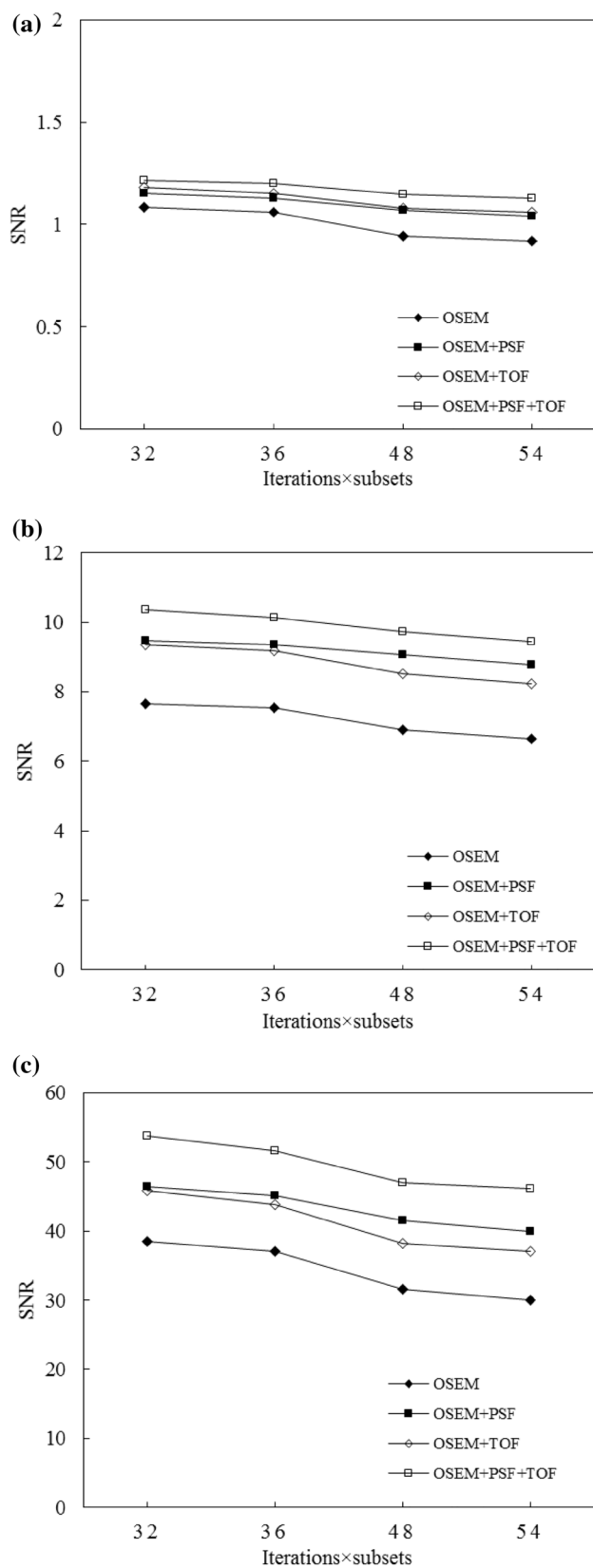


Fig. 6 Comparison of the SNR in various reconstruction protocols for 10 mm diameter sphere of NEMA phantom. The charts represent the SNR vs iterations \times subsets for **a** SBR = 2:1, **b** SBR = 4:1 and **c** SBR = 8:1

and higher $it \times sub$ for all reconstruction protocols (Fig. 3). Furthermore, significant variation for intrinsic FWHM among different protocols was also seen with increase in SBR in the specified $it \times sub$. So for $it \times sub = 54$, the relative difference between OSEM + TOF and OSEM + PSF + TOF was 5.19%, 6.51% and 22.9% when 2:1, 4:1 and 8:1 SBR was applied (Fig. 3). For the phantom study performed by Rogasch et al. [45], noteworthy improvements were also reported when using PSF algorithms especially at high contrast.

It notifies that, in 2:1 SBR, with increase in acquisition time from 1 to 3 min, improvement for intrinsic FWHM was observed for both lower and higher $it \times sub$ (32 and 54); however, nearly the same value was obtained for individual protocols with acquisition time ≥ 3 min to 5 min. Moreover, OSEM + PSF + TOF protocol revealed the best value for intrinsic FWHM among various protocols in our study (Fig. 4). In a recent study, Noto et al. [46] have evaluated the influence of PET acquisition duration on lesion detectability and diagnostic performance. They found that shorter acquisition times (equal to or less than 90 s) resulted in lower image quality as well as lower lesion detectability.

Our results showed that PSF protocols resulted in more variation for intrinsic FWHM in 10 mm sphere size of the NEMA phantom when $it \times sub$ was increased from 32 to 54, for both low and high activity background and SBR; higher differences were seen for higher activity background and SBR (Fig. 5). In general, improved intrinsic FWHM was also seen for higher activity background and SBR with more impact for higher $it \times sub$. Moreover, we found that using OSEM + PSF + TOF algorithm can lead to improving FWHM values for both lower and higher background activities and $it \times sub$ relative to other reconstruction algorithms, in conformity with previous studies [47, 48]. Although further studies focusing on analyzing the detectability in PET images are still required, a better image resolution (i.e., FWHM) has the potential of improving the medical diagnosis of small lesions that can be typically missed, such as early stage tumors, metastatic sites, or small nodules. Previous studies have shown that improving PET spatial resolution can be beneficial in the diagnosis of cancer, e.g., prostate cancer [49].

It can be seen that SNR values decreased by increasing $it \times sub$ for all reconstruction algorithms in all SBRs (Fig. 6), which is attributable to the resulting noise enhancements [50]. The FWHM improvement is notable enough to accept the moderate SNR decrease by increasing $it \times sub$, especially in PSF algorithms. However, on the other hand, our results suggest that more attention must be paid to selection of $it \times sub$ in higher SBRs, specifically if applying non-PSF algorithms.

Some limitations of our study are that all measurements for capillary tubes were done with no background (cold or

warm scattering media) and phantom studies only considered a warm background for all FWHM measurements.

The present work indicates that PET spatial resolution is greatly affected by SBR, background activity and the choice of the reconstruction protocols. We would like to emphasize that FDG avid is different for various cancer with a different type of pathology. For example, bronchoalveolar carcinoma and adenocarcinoma in the lung are not very FDG avid in contrast to diffuse large B-cell lymphoma, follicular lymphoma and squamous cell carcinoma. So it seems various types of cancer can be illustrated with different SBR in the same organ. The distribution of FDG is also different among the human organ (for example, higher uptake in the liver and lower uptake in the lung). It is important to be aware of the lesion size, background activity and type of cancer along with reconstruction protocols for clinical interpretation. Taking into consideration the current results for protocol selection and interpretation in oncologic imaging can improve the accuracy of lesion characterization, in particular in small and low-uptake lesions, and lead to proper clinical interpretation.

Conclusion

Our results demonstrated that spatial resolution in PET images can be related to the SBR, background activity and the choice of the reconstruction protocols. Improvement in spatial resolution can be clearly seen for PSF compared to non-PSF methods when higher $it \times sub$ and SBR are present. In addition, higher variations were seen for high background activities and higher SBR when $it \times sub$ was increased. Furthermore, less variation in spatial resolution can be observed among different protocols by increasing the acquisition time when higher $it \times sub$ was evaluated. Nearly consistent spatial resolutions were observed by increasing acquisition times ≥ 3 min for specific $it \times sub$ and reconstruction protocols.

Funding This work was supported under grant number 33381, Tehran University of Medical Sciences, as well as Masih Daneshvari Hospital and Shahid Beheshti University of Medical Sciences, Tehran, Iran.

Compliance with ethical standards

Conflicts of interest The authors declare that they have no conflict of interest.

References

1. Naqa IE. The role of quantitative PET in predicting cancer treatment outcomes. *Clin Transl Imaging*. 2014;2:305–20.
2. O JH, Jacene H, Lubner B, Wang H, Huynh MH, Leal JP, et al. Quantitation of cancer treatment response by ^{18}F -FDG PET/CT: multicenter assessment of measurement variability. *J Nucl Med*. 2017;58:1429–34.
3. Polycarpou I, Tsoumpas C, King AP, Marsden PK. Impact of respiratory motion correction and spatial resolution on lesion detection in PET: a simulation study based on real MR dynamic data. *Phys Med Biol*. 2014;59:697–713.
4. National Electrical Manufacturers Association. Performance Measurements of Positron Emission Tomographs. NEMA Standards Publication NU 2-2012. Rosslyn: National Electrical Manufacturers Association; 2012. pp 9–11.
5. DeGrado TR, Turkington TG, Williams JJ, Stearns CW, Hoffman JM, Coleman RE. Performance characteristics of a whole-body PET scanner. *J Nucl Med*. 1994;35:1398–406.
6. Goertzen AL, Bao Q, Bergeron M, Blankemeyer E, Blinder S, Canadas M, et al. NEMA NU 4-2008 comparison of preclinical PET imaging systems. *J Nucl Med*. 2012;53:1300–9.
7. Tuna U, Peltonen S, Ruotsalainen U. Gap-filling for the high-resolution PET sinograms with a dedicated DCT-domain filter. *IEEE Trans Med Imaging*. 2010;29:830–9.
8. Loukiala A, Tuna U, Beer S, Jahnke S, Ruotsalainen U. Gap-filling methods for 3D PlanTIS data. *Phys Med Biol*. 2010;55:6125–40.
9. Iriarte A, Marabini R, Matej S, Sorzano CO, Lewitt RM. System models for PET statistical iterative reconstruction: a review. *Comput Med Imaging Graph*. 2016;48:30–48.
10. Cheebsumon P, Yaqub M, van Velden FH, Hoekstra OS, Lamertsmas AA, Boellaard R. Impact of ^{18}F FDG PET imaging parameters on automatic tumour delineation: need for improved tumour delineation methodology. *Eur J Nucl Med Mol Imaging*. 2011;38:2136–44.
11. Prieto E, Dominguez-Prado I, Velloso MJ, Penuelas I, Richter JA, Climent JM. Impact of time-of-flight and point-spread-function in SUV quantification for oncological PET. *Clin Nucl Med*. 2013;38:103–9.
12. Matheoud R, Lecchi M, Lizio D, Scabbio C, Marcassa C, Leva L, et al. Comparative analysis of iterative reconstruction algorithms with resolution recovery and time of flight modeling for ^{18}F -FDG cardiac PET: a multi-center phantom study. *J Nucl Cardiol*. 2017;24:1036–45.
13. Sharifpour R, Ghafarian P, Rahmim A, Ay MR. Quantification and reduction of respiratory induced artifacts in positron emission tomography/computed tomography using the time-of-flight technique. *Nucl Med Commun*. 2017;38:948–55.
14. Akamatsu G, Ishikawa K, Mitsumoto K, Taniguchi T, Ohya N, Baba S, et al. Improvement in PET/CT image quality with a combination of point-spread function and time-of-flight in relation to reconstruction parameters. *J Nucl Med*. 2012;53:1716–22.
15. Rahmim A, Tang J. Noise propagation in resolution modeled PET imaging and its impact on detectability. *Phys Med Biol*. 2013;58:6945–68.
16. Sharifpour R, Ghafarian P, Bakhshayesh-Karam M, Jamaati H, Ay MR. Impact of time-of-flight and point-spread-function for respiratory artifact reduction in PET/CT imaging: focus on SUV. *Tanaffos*. 2017;16:127–35.
17. Rogasch JM, Steffen IG, Hofheinz F, Furth C, Mohnike K, Hass P, et al. The association of tumor-to-background ratios and SUV-max deviations related to point spread function and time-of-flight ^{18}F -FDG-PET/CT reconstruction in colorectal liver metastases. *EJNMMI Res*. 2015;5:31.
18. Andersen FL, Klausen TL, Loft A, Beyer T, Holm S. Clinical evaluation of PET image reconstruction using a spatial resolution model. *Eur J Radiol*. 2013;82:862–9.
19. Vennart NJ, Bird N, Buscombe J, Cheow HK, Nowosinska E, Heard S. Optimization of PET/CT image quality using the GE

- “Sharp IR” point-spread function reconstruction algorithm. *Nucl Med Commun.* 2017;38:471–9.
20. Knausl B, Rausch IF, Bergmann H, Dudczak R, Hirtl A, Georg D. Influence of PET reconstruction parameters on the TrueX algorithm. *Nuklearmedizin.* 2013;52:28–35.
 21. Armstrong IS, Kelly MD, Williams HA, Matthews JC. Impact of point spread function modelling and time of flight on FDG uptake measurements in lung lesions using alternative filtering strategies. *EJNMMI Phys.* 2014;1:99–117.
 22. Soret M, Bacharach SL, Buvat I. Partial-volume effect in PET tumor imaging. *J Nucl Med.* 2007;48:932–45.
 23. Erlandsson K, Buvat I, Pretorius PH, Thomas BA, Hutton BF. A review of partial volume correction techniques for emission tomography and their applications in neurology, cardiology and oncology. *Phys Med Biol.* 2012;57:R119–159.
 24. Kadrmas DJ, Casey ME, Conti M, Jakoby BW, Lois C, Townsend DW. Impact of time-of-flight on PET tumor detection. *J Nucl Med.* 2009;50:1315–23.
 25. Bettinardi V, Castiglioni I, De Bernardi E, Gilardi MC. PET quantification: strategies for partial volume correction. *Clin Transl Imaging.* 2014;2:199–218.
 26. Yan J, Shern JL, Loi HY, Khor LK, Sinha AK, Quek ST, et al. Impact of image reconstruction settings on texture features in ^{18}F -FDG PET. *J Nucl Med.* 2015;56:1667–733.
 27. Kueng R, Driscoll B, Manser P, Fix MK, Stampanoni M, Keller H. Quantification of local image noise variation in PET images for standardization of noise-dependent analysis metrics. *Biomed Phys Eng Express.* 2017;3:025007.
 28. Carlier T, Ferrer L, Necib H, Bodet-Milin C, Rousseau C, Kraeber-Bodéré F. Clinical NECR in ^{18}F -FDG PET scans: optimization of injected activity and variable acquisition time. Relationship with SNR. *Phys Med Biol.* 2014;59:6417–30.
 29. Zeimpekis KG, Barbosa F, Hüllner M, ter Voert E, Davison H, Veit-Haibach P, et al. Clinical evaluation of PET Image quality as a function of acquisition time in a new TOF-PET/MRI compared to TOF-PET/CT-initial results. *Mol Imaging Biol.* 2015;17:735–44.
 30. Lütje S, Blex S, Gomez B, Schaarschmidt BM, Umutlu L, Forsting M, et al. Optimization of acquisition time of ^{68}Ga -PSMA-ligand PET/MRI in patients with local and metastatic prostate cancer. *PLoS ONE.* 2016;11:e0164392.
 31. Umeda T, Miwa K, Murata T, Miyaji N, Wagatsuma K, Motegi K, et al. Optimization of a shorter variable-acquisition time for legs to achieve true whole-body PET/CT images. *Australas Phys Eng Sci Med.* 2017;40:861–8.
 32. Lodge MA, Leal JP, Rahmim A, Sunderland JJ, Frey EC. Measuring PET spatial resolution using a cylinder phantom positioned at an oblique angle. *J Nucl Med.* 2018;59:1768–75.
 33. Hofheinz F, Dittrich S, Pöttsch C, van den Hoff J. Effects of cold sphere walls in PET phantom measurements on the volume reproducing threshold. *Phys Med Biol.* 2010;55:1099–113.
 34. Ketabi A, Ghafarian P, Mosleh-Shirazi MA, Mahdavi SR, Rahmim A, Ay MR. Impact of image reconstruction methods on quantitative accuracy and variability of FDG-PET volumetric and textural measures in solid tumors. *Eur Radiol.* 2019;29:2146–56.
 35. Ketabi A, Ghafarian P, Mosleh-Shirazi M, Mahdavi S, Ay M. The influence of using different reconstruction algorithms on sensitivity of quantitative ^{18}F -FDG-PET volumetric measures to background activity variation. *Iran J Nucl Med.* 2018;26:87–97.
 36. Suljic A, Tomse P, Jensterle L, Skrk D. The impact of reconstruction algorithms and time of flight information on PET/CT image quality. *Radiol Oncol.* 2015;49:227–33.
 37. Taniguchi T, Akamatsu G, Kasahara Y, Mitsumoto K, Baba S, Tsutsui Y, et al. Improvement in PET/CT image quality in overweight patients with PSF and TOF. *Ann Nucl Med.* 2015;29:71–7.
 38. Gong K, Cherry SR, Qi J. On the assessment of spatial resolution of PET systems with iterative image reconstruction. *Phys Med Biol.* 2016;61:N193–N202.
 39. Rahmim A, Qi J, Sossi V. Resolution modeling in PET imaging: theory, practice, benefits, and pitfalls. *Med Phys.* 2013;40:064301.
 40. Lodge MA, Rahmim A, Wahl RL. Simultaneous measurement of noise and spatial resolution in PET phantom images. *Phys Med Biol.* 2010;55:1069–81.
 41. Skretting A. A method for on-site measurements of the effective spatial resolution in PET image volumes reconstructed with OSEM and gaussian post-filters. *Radiat Prot Dosimetry.* 2010;139:195–8.
 42. Lodge MA, Rahmim A, Wahl RL. A practical, automated quality assurance method for measuring spatial resolution in PET. *J Nucl Med.* 2009;50:1307–14.
 43. Yao R, Seidel J, Johnson CA, Witherspoon ME, Green MV, Carson RE. Performance characteristics of the 3-D OSEM algorithm in the reconstruction of small animal PET images. Ordered-subsets expectation-maximization. *IEEE Trans Med Imaging.* 2000;19:798–804.
 44. Yang Y, Tai YC, Siegel S, Newport DF, Bai B, Li Q, et al. Optimization and performance evaluation of the microPET II scanner for in vivo small-animal imaging. *Phys Med Biol.* 2004;49:2527–46.
 45. Rogasch JMM, Hofheinz F, Lougovski A, Furth C, Ruff J, Großer OS, et al. The influence of different signal-to-background ratios on spatial resolution and ^{18}F -FDG-PET quantification using point spread function and time-of-flight reconstruction. *EJNMMI Phys.* 2014;1:12.
 46. Noto B, Büther F, Auf der Springe K, Avramovic N, Heindel W, Schafers M, et al. Impact of PET acquisition durations on image quality and lesion detectability in whole-body ^{68}Ga -PSMA PET-MRI. *EJNMMI Res.* 2017;7(1):12.
 47. Schaefferkoetter J, Casey M, Townsend D, Fakhri GE. Clinical impact of time-of-flight and point response modeling in PET reconstructions: a lesion detection study. *Phys Med Biol.* 2013;58:1465–78.
 48. Akamatsu G, Mitsumoto K, Ishikawa K, Taniguchi T, Ohya N, Baba S, et al. Benefits of point-spread function and time of flight for PET/CT image quality in relation to the body mass index and injected dose. *Clin Nucl Med.* 2013;38:407–12.
 49. Bal H, Guerin L, Casey ME, Conti M, Eriksson L, Michel C, et al. Improving PET spatial resolution and detectability for prostate cancer imaging. *Phys Med Biol.* 2014;59:4411–26.
 50. Shekari M, Ghafarian P, Ahangari S, Ay MR. Quantification of the impact of TOF and PSF on PET images using the noise-matching concept: Clinical and phantom study. *Nucl Sci Tech.* 2017;28:167.